High throughput substrate screening for interfacial thermal management of β-Ga$_2$O$_3$ by deep convolutional neural network ⊕

Special Collection: Machine Learning for Thermal Transport

Mohammed Al-Fahdi [ID] ; Ming Hu ✉ [ID]

Check for updates

View Online   Export Citation

01 June 2024 08:58:00

High throughput substrate screening for interfacial thermal management of β-Ga₂O₃ by deep convolutional neural network ᴱᴾ

Mohammed Al-Fahdi [ID] and Ming Hu[a) [ID]

AFFILIATIONS

Department of Mechanical Engineering, University of South Carolina, Columbia, South Carolina 29208, USA

Note: This paper is part of the special topic, Machine Learning for Thermal Transport.
[a)]Author to whom correspondence should be addressed: hu@sc.edu

ABSTRACT

Electronic devices get smaller and smaller in every generation. In micro-/nano-electronic devices such as high electron mobility transistors, heat dissipation has become a crucial design consideration due to the ultrahigh heat flux that has a negative effect on devices' performance and their lifetime. Therefore, thermal transport performance enhancement is required to adapt to the device size reduction. β-Ga₂O₃ has recently gained significant scientific interest for future power devices because of its inherent material properties such as extremely wide bandgap, outstanding Baliga's figure of merit, large critical electric field, etc. This work aims to use a machine learning approach to search promising substrates or heat sinks for cooling β-Ga₂O₃, in terms of high interfacial thermal conductance (ITC), from large-scale potential structures taken from existing material databases. With the ITC dataset of 1633 various substrates for β-Ga₂O₃ calculated by full density functional theory, we trained our recently developed convolutional neural network (CNN) model that utilizes the fused orbital field matrix (OFM) and composition descriptors. Our model proved to be superior in performance to traditional machine learning algorithms such as random forest and gradient boosting. We then deployed the CNN model to predict the ITC of 32 716 structures in contact with β-Ga₂O₃. The CNN model predicted the top 20 cubic and noncubic substrates with ITC on the same level as density functional theory (DFT) results on β-Ga₂O₃/YN and β-Ga₂O₃/MgO interfaces, which has the highest ITC of 1224 and 1211 MW/m²K, respectively, among the DFT-ITC datasets. Phonon density of states, group velocity, and scattering effect on high heat flux transport and consequently increased ITC are also investigated. Moderate to high phonon density of states overlap, high group velocity, and low phonon scattering are required to achieve high ITC. We also found three Magpie descriptors with strong Pearson correlation with ITC, namely, mean atomic number, mean atomic weight, and mean ground state volume per atom. Calculations of such descriptors are computationally efficient, and therefore, these descriptors provide a new route for quickly screening potential substrates from large-scale material pools for high-performance interfacial thermal management of high-electron mobility transistor devices.

I. INTRODUCTION

In the rapid development of nano- and micro-electronic devices, thermal management is a crucial component to prevent overheating, which might lead to failure, wearout, and the lifetime shortening of the devices. Thermal transport across the interface is a critical part of the thermal dissipation process in those devices.[1–3] The performance of thermal transport between two materials in contact can be measured by the interfacial thermal conductance (ITC) through ITC = Q/ΔT, where Q and ΔT are heat flux and temperature difference between the two materials at the interface, respectively.[1–4] As miniaturization continues, in particular, in nanostructured devices, the characteristic length scales of devices are much shorter than the intrinsic mean free path of phonons in the counterpart bulk materials, and thus, ITC becomes the most important factor for thermal transport. In reality, thermal transport at the interface can be affected by several factors such as binding energy, roughness, and the presence of defects and impurities that

01 June 2024 08:58:00

could occur by the mixture of atoms at intermediate layers at the interface.[5] Phonon reflections caused by the acoustic properties of the adjacent materials take place across the interface even if the two materials are in perfect contact. Therefore, various parameters control ITC, which makes it even more difficult to predict or approximate.[1–6]

Nevertheless, some empirical models have been developed to quickly predict or estimate ITC. Acoustic mismatch model (AMM)[7] and disuse mismatch model (DMM)[8] are the two commonly used ones, and the formulation was presented by Khalatnikov in 1952 and Swartz and Pohl in 1989, respectively. These two models do not take into account the nonequilibrium phonons distribution, instead, they only consider the equilibrium state of phonons,[9,10] which is the case for most heat dissipation situations in electronic cooling. AMM makes a crude simplified assumption about incident phonons undergoing specular transmission and continuum mechanics govern the process. In contrast, DMM assumes that the interface is fully disordered, and therefore, the incident phonons scatter elastically and lose memory after they reach the interface, which might even cause them to scatter back to the source material or transmit into another medium. Moreover, the transmission probability depends on the phonon density of states (DOS). The phonon will scatter into the same phonon energy it once had before reaching the interface which is why some phonons scatter back to the initial material after reaching the interface.[11] In the DMM framework, the phonons that possess frequency ω at mode j and transmit from material A to material B can have ITC as defined below:

$$ITC = \frac{1}{4} \sum_j \int_0^{\omega_{A,j}^v} D_{A,j}(\omega) \frac{\partial n(\omega,\ T)}{\partial T} \hbar \omega v_{A,j} \alpha_{A \to B}(\omega)\ d\omega, \quad (1)$$

where $D(\omega)$ is the phonon DOS at a particular frequency ω, $n(\omega,\ T)$ is the Bose–Einstein distribution of phonons, $\hbar$ is reduced Planck's constant, ω^v is the frequency cutoff, and finally $\alpha_{A \to B}$ is the transmission coefficient from material A to B. The transmission coefficient from material A to material B is further calculated as

$$\alpha_{DMM,A \to B} = \frac{\sum_j D_{B,j} v_{B,j}}{\sum_j D_{A,j} v_{A,j} + \sum_j D_{B,j} v_{B,j}}, \quad (2)$$

where subscripts "A" and "B" mean the materials A and B, respectively, v is the velocity of phonon modes, and the subscript "j" denotes summation over all phonon modes. The DMM model has been widely used in previous studies, and it provides reasonably good results for ITC.

For more accurate ITC computations, more computationally expensive calculations must be implemented such as nonequilibrium molecular dynamics (MD) simulations that naturally consider both harmonic and anharmonic phonon scatterings[12,13] and Green's function method where the phonon anharmonicity can even be considered.[14,15] Despite the shortcomings of DMM compared to experimental results,[16] computational results by DMM are still useful to capture the tendencies in thermal transport across interfaces.[17] More importantly, the DMM offers a fast-screening

approach due to the less expensive computations before experimental synthesis and measurements. However, prediction using the DMM model requires detailed information about the mode level phonon properties such as phonon group velocity and phonon DOS, both of which are not easy to obtain in a high-throughput manner.

The advent of machine learning (ML) and artificial intelligence (AI) has revolutionized many aspects of modern science and technology and has sparked significant interest in the thermal science community in recent years. As a means to make computations even faster, ML algorithms are utilized on data generated by density functional theory (DFT) calculations since they can be utilized to predict various material properties such as mechanical,[18–20] thermal,[21–23] magnetic,[24] and optical[25] properties. In this work, we first performed high-throughput DFT calculations on comprehensive phonon properties of 1633 heat sink materials and then calculated their ITC when being contacted with β-Ga$_2$O$_3$ as a heat source by the DMM model. Here, the β-Ga$_2$O$_3$ was chosen as heat source as a case study since it has recently gained significant scientific interest for future power devices because of its inherent material properties such as extremely wide bandgap, outstanding Baliga's figure of merit, large critical electric field, etc. β-Ga$_2$O$_3$ has been widely used in high-electron mobility transistor (HEMT) applications.[26,27] Using DFT-ITC results as training data, we trained our recently developed convolutional neural network (CNN) model that utilizes the fused orbital field matrix (OFM) and composition Magpie descriptors and then deployed the trained CNN model to predict ITC of large-scale new heat sink materials in contact with β-Ga$_2$O$_3$. This work can be helpful in inverse designing new substrates for HEMT devices that utilize β-Ga$_2$O$_3$ as a heat source.[28,29]

II. WORKFLOW, COMPUTATIONAL DETAILS, AND MACHINE LEARNING MODEL TRAINING

A. Workflow

Figure 1 shows the schematic chart for the entire workflow conducted in this study to accelerate the search for promising substrates or heat sink materials for heat dissipation of β-Ga$_2$O$_3$. The first step is to obtain the structures from the open quantum material database (OQMD), and we re-optimized them with our own DFT parameters (see computational details of DFT calculations below). Then, the second- and third-order interatomic force constants (IFCs) of the majority of structures were obtained from our previous works[21–23,30–32] with a small amount of additional DFT calculations utilizing the same compression sensing lattice dynamics (CSLD) method to calculate the phonon dispersions. The second-order IFCs confirm the dynamic stability through the absence of negative phonon frequencies in the Brillouin zone. Then, almaBTE calculations using both second- and third-order IFCs of materials as input are performed to create a dataset for β-Ga$_2$O$_3$/X interfaces having ITC as target (here "X" denotes a substrate or heat sink material in contact with β-Ga$_2$O$_3$). The dataset is then used to train our developed fused OFM + Magpie CNN model, and subsequently, the model is used to make ITC predictions on new candidate substrates in contact with β-Ga$_2$O$_3$. For the screening pool, we prepared 32 716 structures with non-zero
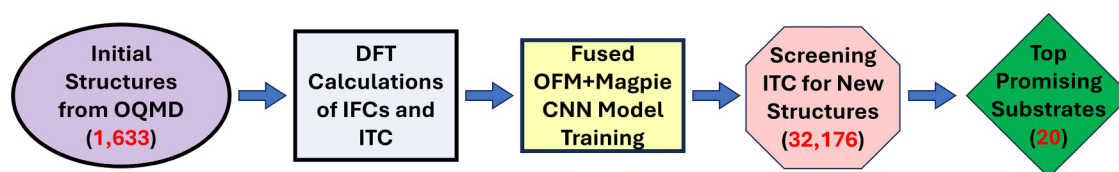
FIG. 1. Step-by-step schematic chart for the workflow used in this work to accelerate searching potential substrates for cooling β-Ga$_2$O$_3$. The entire workflow is composed of (1) re-optimization of 1633 structures taken from OQMD database; (2) full DFT calculations of second- and third-order interatomic force constants (IFCs) and interfacial thermal conductance (ITC) between the 1633 structures and β-Ga$_2$O$_3$; (3) fused OFM + Magpie convolutional neural network (CNN) model training by using the 1633 DFT-ITC datasets; (4) deployment of the trained CNN model to predict ITCs of 32 716 structures with non-zero bandgap in contact with β-Ga$_2$O$_3$; (5) finally top 20 promising substrates for interfacial thermal management of β-Ga$_2$O$_3$ are suggested.

bandgap as a special requirement for thermal management applications. All 32 716 structures were screened out from the OQMD database and have been successfully re-optimized by DFT calculations with our own computational parameters. The structures that were not successfully optimized were discarded.

B. DFT calculations

All the 1633 crystal structures used for training our developed fused OFM + Magpie CNN model are downloaded from the OQMD database in crystallographic information file (CIF) format.[33] All the structures were re-optimized by first-principles DFT calculations utilizing Vienna *Ab-Initio* Simulation package.[34–36] For re-optimizing the structures, we use their primitive cells with total energy and force convergence criteria of 10^{-8} eV and 10^{-4} eV/Å, respectively. The atomic positions, cell shape, and sizes of the primitive cells are all allowed to change in the re-optimization process to reach the minimum energy in each structure. The Perdew–Burke–Ernzerhof (PBE)[37] is selected from the generalized gradient approximation (GGA) to characterize the exchange-correlation effects of electrons within the linear projector augmented wave (PAW) generalization of the pseudopotentials method[38] to allow DFT to perform calculations with higher efficiency. The kinetic energy cutoff of 520 eV was selected to limit the number of plane waves utilized as basis functions at each wavevector in the k-space. The Monkhorst–Pack k-mesh was applied to sample the Brillouin zone.[39] The number of k-points for electrons was determined such that the multiplication between the lattice vector and the number of k-points is at least 60 at each lattice vector to ensure high-quality k-mesh. After primitive cells were re-optimized, supercells were generated based on the optimized primitive cells, in which each atom was randomly displaced by a displacement of 0.03 Å. For each primitive cell, 16–30 supercells were generated, with a detailed number of supercells depending on the symmetry of the materials. The atomic forces of the supercells were then evaluated by VASP calculation with energy and force convergence criteria of 10^{-6} eV and 10^{-4} eV/Å, respectively. After that, the second-order (harmonic) and third-order (anharmonic) interatomic force constants (IFC) were generated using the compressive sensing lattice dynamics (CSLD) method,[40–42] and the IFCs were output in Phonopy[43] format. ShengBTE package was then utilized to obtain the lattice thermal conductivity (LTC)[44] through an iterative method. The LTC of β-Ga$_2$O$_3$ was calculated

by our DFT + BTE to be 11.6, 20, and 16.6 W/mK in the [100], [010], and [001] direction, respectively, which are in good agreement with those reported in Ref. 45. With second- and third-order IFCs, the almaBTE package[46] was utilized to approximate the interfacial phonon transmission coefficient using the DMM model and subsequently obtain ITC through Monte–Carlo simulations. In the almaBTE calculations, two slabs composed of β-Ga$_2$O$_3$ as the heat source and another substrate as the heat sink were set up, with each slab of 100 nm thick. It should be noted that, since β-Ga$_2$O$_3$ is a highly anisotropy material, the ITC would depend on the specific axis or orientation chosen when running almaBTE. After testing all three cartesian axes, we find that the heat transport along [010] cartesian axis yields the highest ITC, which can be understood in terms of the highest LTC in the same direction. Therefore, all ITC results presented in this work refer to the orientation of [010] for β-Ga$_2$O$_3$. For the phonon wavevector **q** in the almaBTE calculations, 50 q-point line density for each lattice vector was implemented. The simulation temperature difference between the heat source and heat sink is 5 K. The number of particles in the simulation is 1×10^6, which is large enough after testing. The temperature is output on 300 equally spaced bins sliced perpendicularly to the heat flux direction in the two slabs. The ITC between β-Ga$_2$O$_3$ and the substrate is calculated by the temperature difference at the interface.

C. CNN model construction and training

Figure 2 shows the schematic chart for our recently developed fused orbital field matrix (OFM) + Magpie CNN model. OFM[47] is based on the representation of the valence shell electrons of a local chemical environment by considering the sum of the weighted vector of all atoms in that environment. More details on the OFM calculation method can be learned from Ref. 47. Magpie features[48] are statistical results of maximum, minimum, mean range, and mode of the elemental descriptors generated based on the composition of the material. OFM and magpie descriptors do not require expensive computations to acquire them. Matminer[49] can generate such descriptors for thousands of materials in less than 1 s. The layer numbers shown in red color are for both OFM[47] and Magpie[48] descriptors. The OFM we used is a 32×32 matrix or second-rank tensor. Such matrix can be used as an input for a 2D CNN as seen in the conv2D in Fig. 2 layer 1 and layer 2(b) shown in the texts in red color. The feature matrix from the two separate
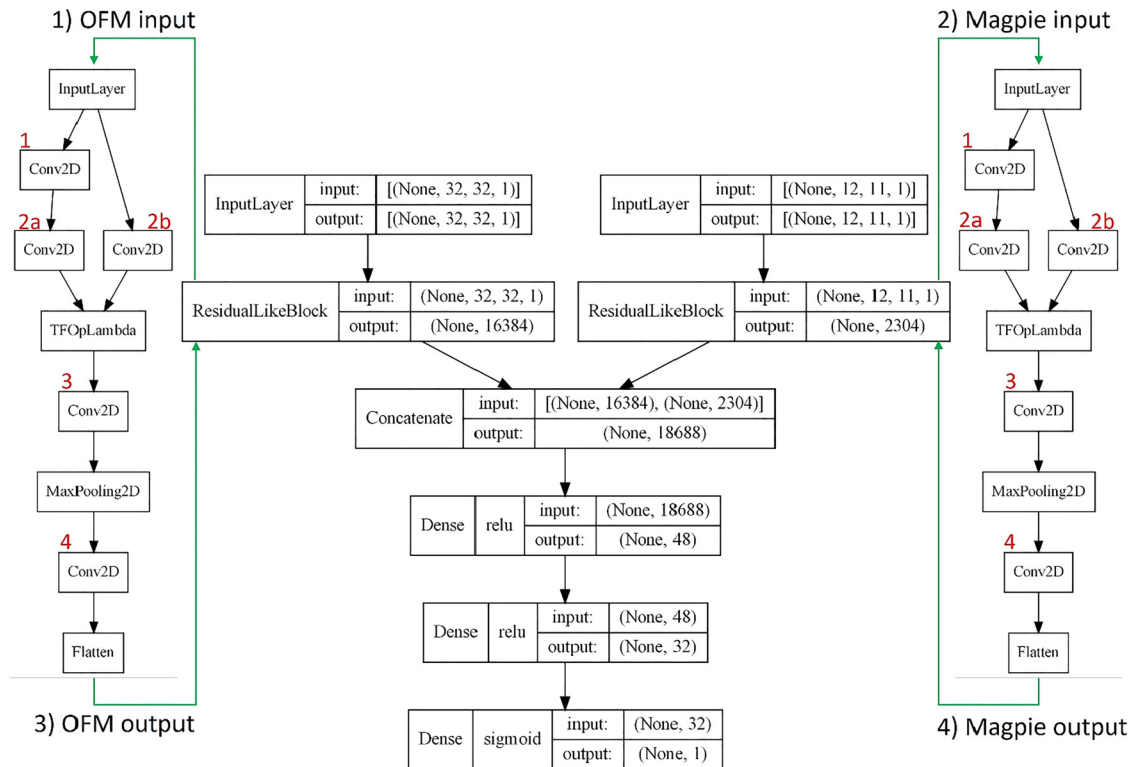
01 June 2024 08:58:00

FIG. 2. Schematic chart of the regression architecture of the fused OFM + Magpie CNN model to predict ITC. The orbital field matrix (OFM) input matrix is 32 × 32 as seen from label (1) OFM input, and the output features from OFM are 16 384 as seen from label (3) OFM output. The number of kernels in OFM "ResidualLikeBlock" from the Conv2D layers numbered in red: 1–5, 2a–3, 2b–3, 3, 4–3, and the number of filters is 1–32, 2a–32, 2b–32, 3–64, 4–64 with the MaxPooling2D size of (2, 2). The input matrix for Magpie is 12 × 11 as seen from the label (2) Magpie input step, and the output features for Magpie are 2304 as seen from label (4) Magpie output step. The number of kernels in magpie "ResidualLikeBlock" from the Conv2D layers numbered in red: 1–3, 2a–3, 2b–3, 3–3, 4–3, and the number of filters is 1–32, 2a–48, 2b–48, 3–64, 4–64 with the MaxPooling2D size of (2, 2). OFM and Magpie output features (i.e., 18 688 features in total) are both fused or merged and used as input into the first dense layer with 48 features before passing to the other dense layer of 32 output features then to the last dense layer that makes the prediction.

path conv2D in layer 2(a) and layer 2(b) is combined and proceeds to go to conv2D in layer 3 and then max pooled before going through another conv2D shown indicated by the red number 4. The number of kernels in OFM forward propagation conv2d layers is as follows from the red numbers in the "ResidualLikeBlock": 1–5, 2a–3, 2b–3, 3, 4–3. The number of filters in OFM forward propagation Conv2d layers is as follows: 1–32, 2a–32, 2b–32, 3–64, 4–64. In the magpie forward propagation Conv2D layers, the number of kernels is as follows: 1–3, 2a–3, 2b–3, 3–3, 4–3, and the number of filters is as follows: 1–32, 2a–48, 2b–48, 3–64, 4–64. The ReLU activation function is used in all the conv2d layers and dense layers except for the last dense layer that has no activation function. The padding is the "same" in all the conv2D layers. The pool size is (2, 2) in the MaxPooling2D layer. The 2D feature matrix is then flattened to become a feature vector that has the shape of 16 384. The Magpie descriptors can be represented as a 132-feature vector and can be shaped into a 12 × 11 matrix to be used as an input to a conv2D. The Magpie matrix follows a similar path of layers before flattening and becomes a feature vector that has the shape of 2304.

The flattened feature vector from the OFM path and flattened feature vector from the Magpie path are then concatenated before progressing to three dense layers to make a prediction on ITC of substrates in contact with β-Ga_2O_3. The model is to train the 1633 materials dataset. The 1633 materials dataset is split into 80%/10%/ 10% for training, validation, and testing sets, respectively. The learning rate used in the AdamW optimizer is 0.001. A similar model was used in this work.[50] However, the model was used for classification not regression as in this work. The entire model flow-chart is built on Tensorflow.[51]

III. RESULTS AND DISCUSSION

Figure 3(a) shows the training and validation losses with respect to the number of training epochs. The loss function in each epoch is the mean absolute error (MAE) loss function as implemented from Tensorflow. The maximum number of epochs is 60 epochs, which is more than enough to reach the lowest loss. As a matter of fact, the model plateaus do not significantly reduce the
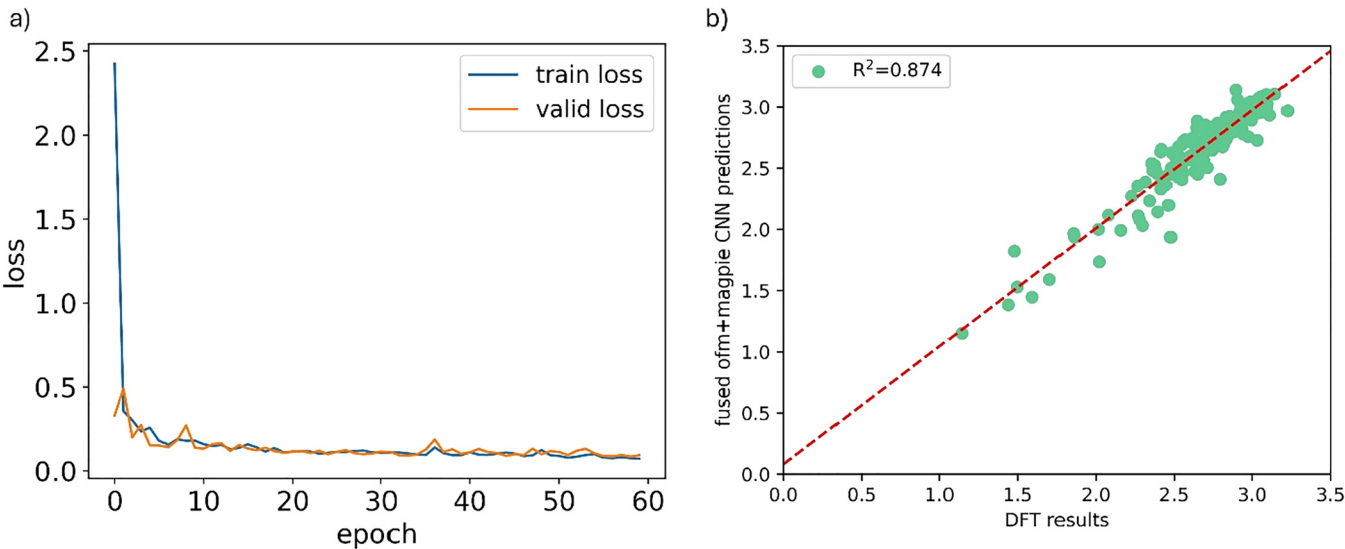
01 June 2024 08:58:00

FIG. 3. (a) Training and validation losses of fused OFM + Magpie CNN model on the DFT calculated 1633 ITC data. (b) Comparison of ITC between DFT-ITC results and the fused OFM + Magpie CNN predictions. The ITCs are base 10 logarithm values in unit of log(MW/m^{2}K). The red dashed line shows R^2 line as guidance.

loss after the tenth epoch, which means the model training converges very fast. In Fig. 3(b), we compare the ITC in base 10 logarithm values between full DFT calculations and prediction by the fused OFM + Magpie CNN model with R^2 score labeled. Generally speaking, the R^2 score of an ML model prediction should be as high as possible (e.g., close to unity) since the metric denotes the consistency of the results from testing or the model's previously unseen dataset of ITC values compared to the predictions by the model. The R^2 score of our trained fused OFM + Magpie CNN model is as high as 0.874, which confirms that our fused OFM + Magpie CNN model is well trained with high quality and can, thus, be utilized to predict ITCs for new or previously unseen substrates in contact with β-Ga$_2$O$_3$.

Since there are many previously widely used ML models available, then it is worth comparing our fused OFM + Magpie CNN model with those models to affirm its superiority in ITC predictions. To this end, our regression results from the fused OFM + Magpie CNN model are compared with two well-known and traditional ML models: (1) gradient boosting (GB)[52] and (2) random forest (RF).[53] Both ML models used the Magpie

descriptors to train their respective models. These two ML algorithms are imported from sci-kit learn library.[54] The comparison among the three models is implemented by comparing the metrics among the models, i.e., R^2 score and MAE. Table I shows the comparison results of the metrics among the three trained models. The R^2 score of our developed fused OFM + Magpie CNN model is the highest among three ML models. MAE should be as low as possible to substantiate that model's prediction (i.e., predicted ITC) is not far off from the true value (i.e., "true" ITC). We find that the MAE of our developed CNN model is the lowest among the three models. From these two metrics, we can conclude and affirm that our developed CNN model has superior performance and tremendous capability compared to the other two traditional ML algorithms in predicting ITC of substrates in contact with β-Ga$_2$O$_3$.

With the well-trained fused OFM + Magpie CNN model, we continue to deploy the model to predict the ITC of 32 716 structures in contact with β-Ga$_2$O$_3$. Figure 4 shows the statistical distribution of the ML dataset of 1633 DFT materials and 32 716 materials in the prediction dataset in terms of the number of atoms, mass density, and volume of primitive cells. The prediction pool is much larger and contains a wider range of structures compared to the ML dataset that was used to train, validate, and test the ML model. Here, we need to emphasize that the ITCs in base 10 logarithm values were first predicted, and then they were converted back to the normal values in units of MW/m^{2}K. The top 10 structures with the highest predicted ITCs as promising substrates for cooling β-Ga$_2$O$_3$ are presented in Tables II and III, respectively. Relevant structure information such as formula, bandgap, formation energy, etc., are also provided. Interestingly, all top 10 cubic substrates happen to have the same space group number of 227 and the same prototype AB$_2$C$_4$, although our screening pool includes lots of materials with other space group numbers such as

TABLE I. Comparison of the performance among the three trained machine learning models. The MAE is measured based on ITCs in base 10 logarithm values.

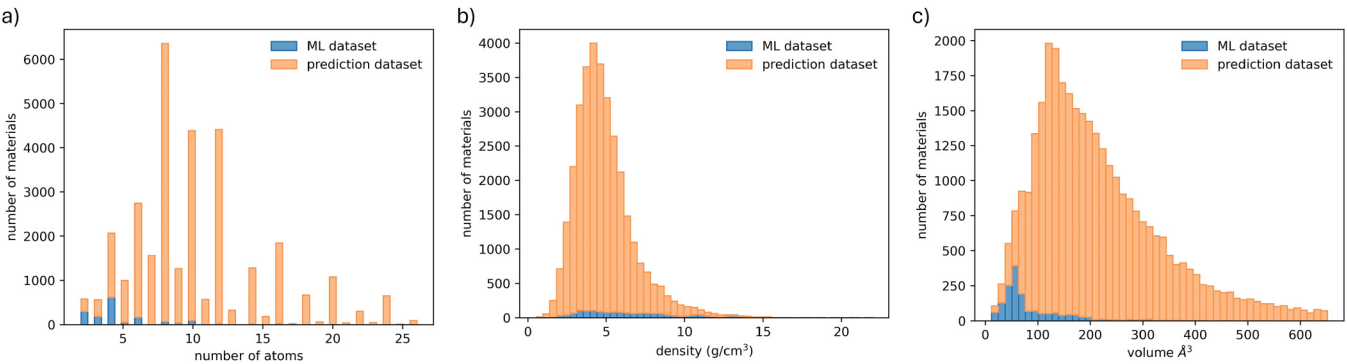| Metrics	Fused OFM + Magpie CNN model	Gradient boosting model	Random forest model
R^2	0.874	0.801	0.689
Mean absolute error (MAE)	0.0872	0.0943	0.1198

FIG. 4. Statistical distribution of number of atoms, mass density, and volume of primitive cells for ML dataset and prediction pool.

TABLE II. Top 10 cubic structures with highest ITC in contact with β-Ga$_2$O$_3$ predicted by our developed Fused OFM + Magpie CNN model. Relevant material information are also provided. The bandgap values are taken from original OQMD database.

| OQMD ID	Formula	Bandgap (eV)	Formation energy (eV/atom)	Prototype	Space group no.	Predicted ITC (MW/m^{2}K)
1 283 850	MnAl$_2$O$_4$	2.87	−2.958	AB$_2$C$_4$	227	1207.6
4643	Al$_2$ZnO$_4$	4.16	−2.864	AB$_2$C$_4$	227	1124.3
6015	MgAl$_2$O$_4$	5.53	−3.230	AB$_2$C$_4$	227	1090.7
432 196	Sc$_2$CdO$_4$	3.17	−3.085	AB$_2$C$_4$	227	1041.0
675 547	Mn(GaO$_2$)2	1.79	−2.134	AB$_2$C$_4$	227	999.8
1 283 764	Mg$_2$SiO$_4$	5.22	−3.013	AB$_2$C$_4$	227	987.5
30 721	Mg(RhO$_2$)2	1.17	−1.501	AB$_2$C$_4$	227	968.1
1 284 057	Y$_2$CoO$_4$	2.90	−2.914	AB$_2$C$_4$	227	921.8
19 125	Co(RhO$_2$)2	0.84	−1.060	AB$_2$C$_4$	227	897.7
432 150	CaY$_2$O$_4$	4.43	−3.593	AB$_2$C$_4$	227	891.1

TABLE III. Top 10 noncubic structures with highest ITC in contact with β-Ga$_2$O$_3$ predicted by our developed Fused OFM + Magpie CNN model. Relevant material information are also provided. The bandgap values are taken from original OQMD database.

OQMD ID	Formula	Bandgap (eV)	Formation energy (eV/atom)	Prototype	Space group no.	Predicted ITC (MW/m^{2}K)
6270	Al$_2$PbO$_4$	4.03	−2.736	AB$_2$C$_4$	9	1436.5
1 385 886	LiScO$_2$	4.29	−3.178	ABC$_2$	62	1335.6
1 386 734	NaIrO$_2$	1.53	−1.191	ABC$_2$	166	1329.8
5699	LiRhO$_2$	1.55	−1.426	ABC$_2$	166	1328.2
31 809	LiCoO$_2$	2.50	−1.693	ABC$_2$	166	1295.0
3724	LiGaO$_2$	3.53	−2.241	ABC$_2$	33	1289.4
711 441	NaGaO$_2$	3.17	−2.112	ABC$_2$	33	1283.5
1 347 988	RbAlO$_2$	4.23	−2.741	ABC$_2$	92	1282.5
1 234 774	Al$_2$O$_3$	6.31	−3.265	A$_2$B$_3$	167	1274.5
1 278 107	Si$_2$O$_3$	1.28	−2.247	A$_2$B$_3$	148	1274.5

TABLE IV. Pearson correlation results of elemental features with ITC.

Features	Pearson correlation
Mean atomic number	−0.4995
Mean atomic weight	−0.4987
Mean GS volume PA	−0.4637

225, 221, and 216, and other prototypes as well such as AB, ABC, ABC_2, ABCD, etc. This means similar atomic structure and other similar structural features will likely lead to similar ITC, as we will see shortly from the analysis of DFT-ITC data. In contrast, the top 10 noncubic substrates have slightly diverse space groups and prototypes, primarily because there are many more space groups and prototypes in the screening pool. Again, similar material families in
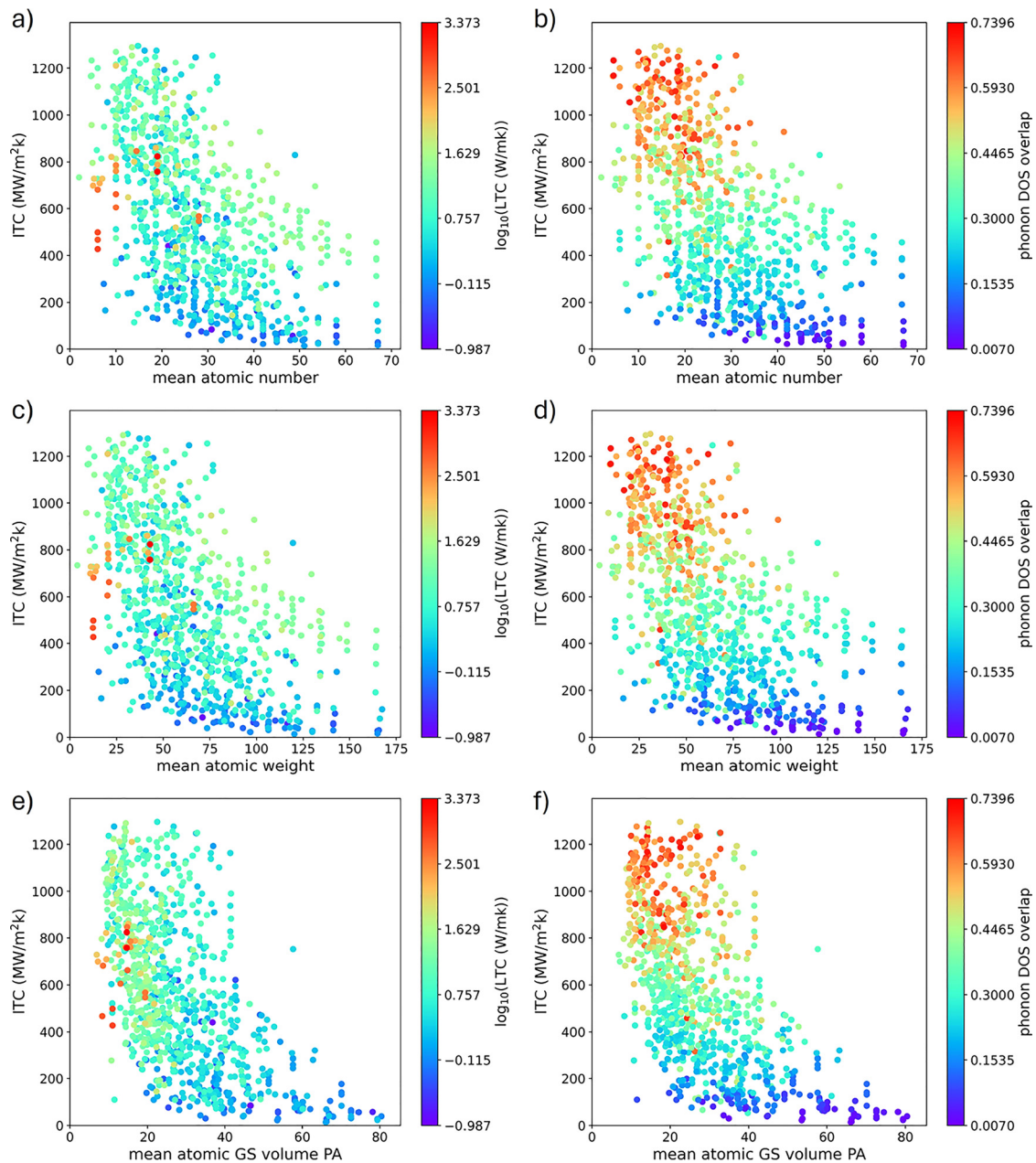
FIG. 5. Dependence of ITC on elemental descriptors: (top) mean atomic number, (middle) mean atomic weight, and (bottom) mean atomic ground state (GS) volume per atom (PA) color mapped with LTC (left panel) and phonon DOS overlap (right panel) of 1633 DFT materials dataset that was used for training, validation, and testing of ML models.

particular with the same prototype and close average atomic mass tend to have similar ITCs.

Since we have prepared many Magpie atomic descriptors for all structures in our training dataset during traditional ML training, it is then intuitive to calculate the Pearson correlation coefficients[55] of ITC with those Magpie atomic descriptors. Pearson correlation values range from −1 to +1. Positive (negative) values denote a directly proportional (inverse) correlation between two variables. The high value of Pearson correlation regardless of the sign (i.e., close to +1 or −1) indicates a strong correlation between the two variables, while the Pearson correlation coefficient close to zero, regardless of the sign, denotes a weak or no correlation between two parameters. The three Magpie descriptors selected to show in Table IV are the mean atomic number, mean atomic weight, and mean ground state (GS) volume per atom (PA), which have the highest Pearson correlation coefficients of −0.4995, −0.4987, and −0.4637, respectively, among the total 132 Magpie descriptors we have studied. The coefficients are represented in absolute value because the strength of the correlation coefficient is one of the crucial factors to correlate with ITC regardless of the sign. The reason why these descriptors have high Pearson correlation coefficients is because the constituent species in β-Ga$_2$O$_3$ all have medium to low atomic weights, which means the material possesses phonon states at high frequencies in its phonon dispersion in the reciprocal space.[56,57] As implied in Eqs. (1) and (2), similar vibrational frequencies between the heat source and substrate are one of the crucial factors in acquiring high ITC. Therefore, materials with medium to low atomic weight or atomic number should have high frequencies and possibly high phonon DOS overlap with β-Ga$_2$O$_3$. Regarding the high Pearson correlation coefficient for the mean GS volume per atom, it is due to the light elements having low GS volume per atom, and those light elements also tend to have high frequencies in their phonon dispersions. Therefore, the mean GS volume per atom descriptor happens to have the same trend in the periodic table as the atomic weight, which made its correlation high with ITC. The same analysis for the mean GS volume per atom can be applied to other descriptors such as covalent radius because it follows the same periodic table trend.

According to Table IV, the mean atomic number, mean atomic weight, and mean atomic GS volume PA are highly and negatively correlated with ITC according to their high negative Pearson correlation coefficients. Those descriptors can visually explain and give insights on ITC in Fig. 5 by adding LTC and phonon DOS overlap as comparison parameters because phonon DOS overlap is directly correlated with ITC according to Eqs. (1) and (2). Furthermore, the phonon DOS overlap between the heat source and heat sink is crucial for DMM as stated in Refs. 8 and 11. Regarding LTC, even if LTC is not directly correlated with ITC, phonon group velocity and three phonon scatterings are necessary factors to consider in computing LTC. As group velocity becomes high and phonon scatterings become low, LTC should be high, and vice versa. Therefore, if LTC is high in the substrate, ITC should go up consequently. Inspired by Eqs. (1) and (2), the phonon DOS overlap in this study is quantitatively characterized as
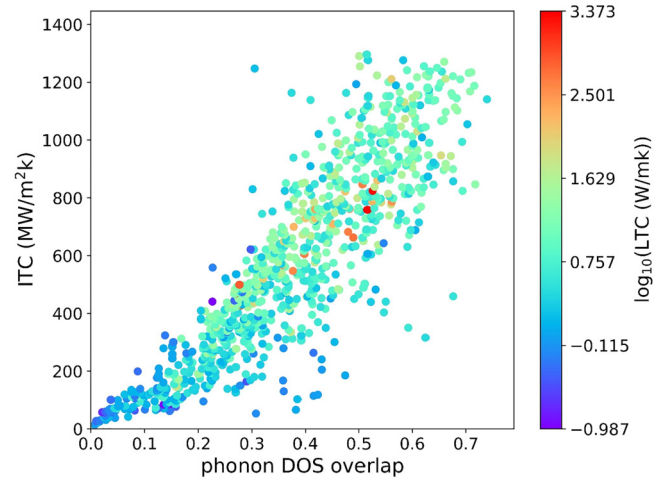

FIG. 6. Dependence of ITC on phonon DOS overlap between β-Ga$_2$O$_3$ and 1633 substrates by high throughput DFT calculations. The color is mapped by the LTC values of substrates in base 10 logarithm.

$$\text{Phonon DOS Overlap} = \frac{2\int_0^\infty D_{overlap}(\omega)d\omega}{\int_0^\infty D_{heat\ source}(\omega)d\omega + \int_0^\infty D_{substrate}(\omega)d\omega},$$

(3)

where $D_{overlap}$ is the phonon DOS in the overlap region between the substrate and heat source. In practice, the integral was conducted up to the higher cutoff frequency of the substrate and heat source (β-Ga$_2$O$_3$). The initial visual take on all panels from the three descriptors in Fig. 5 without even considering LTC and phonon DOS overlap is that as mean mass, mean atomic number, and mean GS volume PA decrease, the ITC increases. That further substantiates the negative correlation results found from Table IV. The explanation is essentially due to the similar phonon density of states between β-Ga$_2$O$_3$ and other substrates with low to average mean atomic number or weight. It can be seen from Fig. 5 panels (a), (c), (e) that generally speaking the higher LTC is commensurate with higher ITC because blue-colored data points with low LTC exist at the bottom where ITC is low. On the other hand, colors with higher LTC in the color bars exist at higher ITC in general. Regarding phonon DOS overlap in Fig. 5 panels (b), (d), and (f), substrates with higher phonon DOS overlap with β-Ga$_2$O$_3$ tend to have higher ITC. Comparing left and right panels in Fig. 5, the phonon DOS overlap trend from right panels is more obvious. That implies if a substrate with extremely high LTC but not vibrationally similar to β-Ga$_2$O$_3$, the ITC is highly expected to be low. The previous results confirm the theory that ITC requires higher phonon DOS overlap between the heat source and its substrate along with higher group velocity and less phonon scatterings.

From Table IV and Fig. 5, it is confirmed that ITC is inversely proportional to the similarity in atomic number or atomic mass, which comes from the vibrational similarity or phonon DOS

overlap between β-Ga$_2$O$_3$ and the substrate. Therefore, we continue to quantitatively investigate the relationship between ITC and phonon DOS overlap. Figure 6 manifests ITC values of β-Ga$_2$O$_3$ with other substrates along with phonon DOS between β-Ga$_2$O$_3$ and those substrates. LTC of the substrates is added as a color map to the analysis since it adds a measure for the phonon group velocity of the substrate, which is also another crucial parameter for ITC. The clear and obvious trend that can be seen from Fig. 6 is that ITC is equal to zero if phonon DOS overlap between β-Ga$_2$O$_3$ and another substrate is also equal to zero, which is well expected under the assumption of the DMM model used by the almaBTE package. This analysis and results are completely understandable since Eqs. (1) and (2) reveal that zero phonon DOS overlap should

have zero ITC as well. In other words, phonon DOS overlap must not be zero in order to make a nonzero or finite ITC. It is also shown from the bottom-right region in Fig. 6 that, although phonon DOS overlap is a bit high between 0.3 and 0.6, the ITC is relatively low. This is because the LTCs of most substrates are low (the corresponding LTC color is dark blue). That could also convey that those substrates have low group velocity and as a result low ITC. In that same range (i.e., phonon DOS overlap from 0.3 to 0.6), the data higher than the bottom-right (i.e., higher ITC) have higher LTC as indicated by the color in the LTC color bar. This indicates that higher LTC leads to higher ITC for the same phonon DOS overlap, which can be explained by the fact that the higher LTC usually has high group velocity and consequently higher ITC.
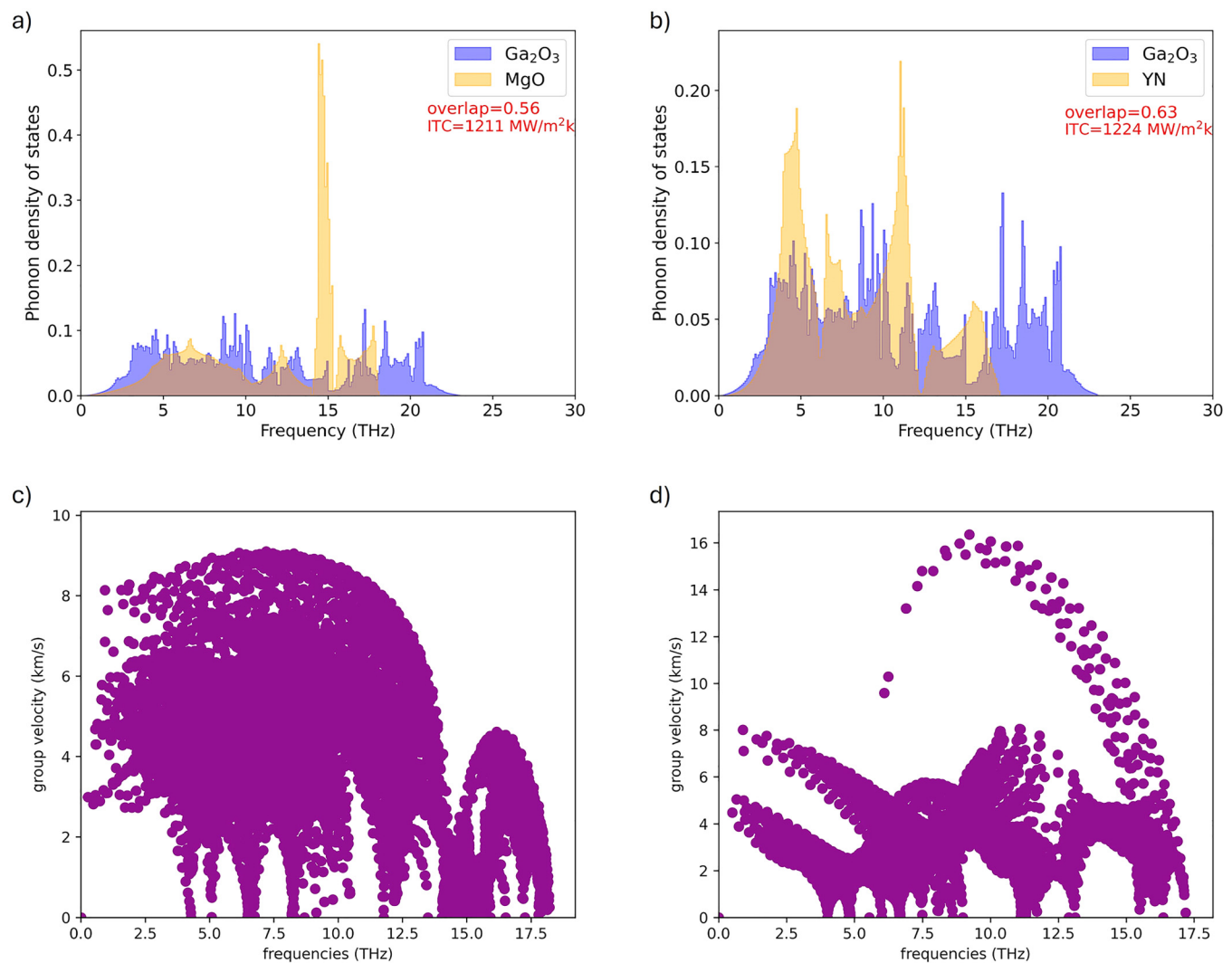
FIG. 7. Phonon DOS overlap between substrate (a) MgO, (b) YN, and heat source β-Ga$_2$O$_3$. The purple and yellow color represents phonon DOS of β-Ga$_2$O$_3$ and substrate, respectively. The gray area portrays the phonon DOS overlap between β-Ga$_2$O$_3$ and substrate. Panels (c) and (d) illustrate the phonon frequency dependent group velocity of MgO and YN, respectively.

However, this trend is not always true. In Fig. 6, we find that there are lots of substrate materials with very high ITC when being contacted with β-Ga₂O₃, but those materials do not necessarily have high LTC. Specifically, for ITC above 800 MW/m²K, many substrates only have moderate to low LTC values, roughly in the range from 10 to 30 W/mK. The high ITC is then primarily resulted from the high phonon DOS overlap. Overall, the results in Fig. 6 demonstrate that for heat sources with low LTC like the case of β-Ga₂O₃ (the LTCs in three directions are between 10 and 20 W/mK obtained by our DFT calculations), the phonon DOS overlap between two neighboring materials is much more important than the LTCs of substrates themselves in terms of achieving high ITC at the interfaces.

Since the high phonon DOS overlap is a necessary condition to obtain high ITC between a heat source and substrate as understood from Eqs. (1) and (2) and visually portrayed in Fig. 6, particularly for two contacting materials with low LTC, in Fig. 7, we show two representative examples, (a) namely, MgO and (b) YN, of the phonon DOS overlap with β-Ga₂O₃. These two substrates were chosen because their ITCs are the highest among all 1633 DFT-ITC datasets. Specifically, the ITC for β-Ga₂O₃/MgO and β-Ga₂O₃/YN interface is as high as 1211 and 1224 MW/m²K, respectively. It can be seen from Fig. 7 that high phonon DOS overlap exists between β-Ga₂O₃ and the two substrates, with the calculated values of 0.56 and 0.63 for β-Ga₂O₃/MgO and β-Ga₂O₃/YN interface, respectively. The phonon DOS overlap spans acoustic and optical phonon branches. Moreover, the phonon group velocity seems to be high in MgO in the acoustic branch and most of the phonon modes in the optical branch except for those from 15 to 17.5 THz, as shown in Fig. 7(c). A similar phenomenon is observed in YN where high phonon group velocity is observed in Fig. 7(d) for all phonon modes, particularly for some optical phonon modes with frequency above 7.5 THz.

Although Fig. 7 shows the phonon modes that possibly contribute to transporting heat from the phonon DOS overlap and the high group velocity phonon region that might transport more heat across the interface, it does not quantitatively tell us which phonon modes can actually transport how much heat across the interface, since transmission coefficient is another very important factor to interfacial thermal transport according to Eqs. (1) and (2). Besides, almaBTE considers several scattering mechanisms such as intrinsic phonons scattering, interface scattering, and absorption scattering. Therefore, even with phonon DOS overlap and high group velocity, the scattering mechanisms implemented in almaBTE might hinder transporting higher heat fluxes. To this end, Fig. 8 shows which phonon modes and frequencies transport how much heat. For the β-Ga₂O₃/MgO interface shown in Fig. 8(a), phonon frequencies from around 0.5 THz to roughly 8 THz transport the highest amount of heat compared to other phonon modes that overlap between 8 and 17 THz. That can be explained by the high group velocity in the acoustic branches and less phonon scattering compared to the higher frequency phonon modes in the optical branches, which might have high phonon group velocity in most of the states but high phonon scatterings as well. For β-Ga₂O₃/MgO interface shown in Fig. 8(b), high heat flux is transported by the phonons with frequency between 0 and 9 THz, which indicates the higher group velocities at those frequencies and less phonon scattering. Similar to the β-Ga₂O₃/MgO interface, although there is a large overlap between those two materials for phonon states from 9 to 17 THz, these phonon modes do not contribute much to transporting a significant amount of heat flux, which is mainly due to high phonon scattering at those phonon states. Overall, the spectral heat flux analysis in Fig. 8 demonstrates that the high phonon DOS overlap and high phonon group velocity along with low scattering rates are required for achieving high ITC.
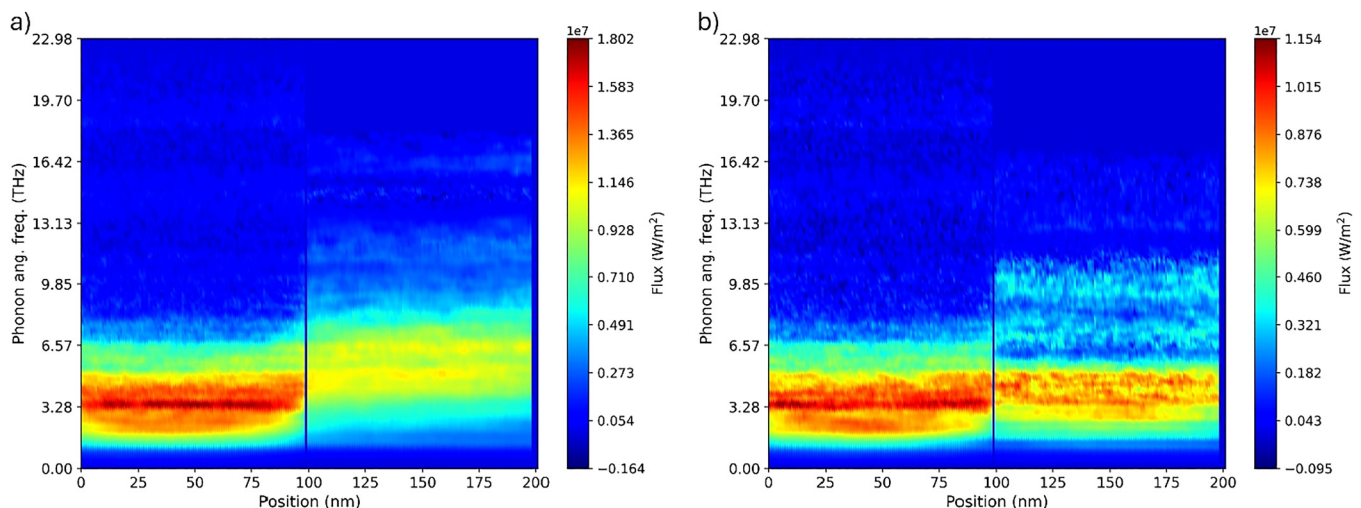
FIG. 8. Phonon frequency resolved spectral heat flux of (a) MgO and (b) YN in contact with β-Ga₂O₃. The left 100 nm region corresponds to β-Ga₂O₃ (heat source) while the right 100 nm region is the substrate (heat sink), i.e., (a) MgO and (b) YN.

IV. CONCLUSION

In summary, the objective of this work is to accelerate screening suitable substrates for cooling β-Ga$_2$O$_3$, a common material used in HEMT devices. The potential substrate candidates should have high ITC in contact with β-Ga$_2$O$_3$ to dissipate as much heat as possible to prevent the devices from wearing out and to prolong their lifetime. To this end, the ITC of 1633 substrates in contact with β-Ga$_2$O$_3$ is calculated using almaBTE with the required second- and third-order IFCs computed directly from high-accuracy DFT calculations. DFT-ITC results reveal that the phonon DOS overlap plays an important effect on the ITC, and the phonon DOS overlap of about 0.3 or higher is a necessary condition to achieve high ITC. Group velocity plays another crucial role in attaining high ITC. For phonons in the finite (non-zero) DOS overlap region, the phonon group velocity becomes one of the dominant factors for ITC. The third factor affecting ITC is the scattering at the interface. Even for the phonon modes at various frequencies that overlap between β-Ga$_2$O$_3$ and a specific substrate, it is not guaranteed that high heat flux can be transported across the interface by those modes since they might have strong scatterings. The β-Ga$_2$O$_3$/YN and β-Ga$_2$O$_3$/MgO interfaces possess the highest ITC of 1224 and 1211 MW/m^{2}K, respectively, among the 1633 DFT-ITC datasets. Both substrates fulfill the three governing factors or requirements mentioned above, namely, high phonon DOS overlap, high group velocity, and weak scatterings. With 1633 DFT-ITC datasets, we trained our recently developed convolutional neural network model that utilizes the fused orbital field matrix and composition descriptors. Our model proved to be superior in performance to traditional machine learning algorithms such as random forest and gradient boosting. We further deployed the CNN model to predict the ITC of 32 716 structures with non-zero bandgap in contact with β-Ga$_2$O$_3$. The CNN model predicted the top 20 cubic and noncubic substrates with ITC on the same level (around 1000 MW/m^{2}K) as Ga$_2$O$_3$/YN and β-Ga$_2$O$_3$/MgO interface. We also performed Pearson correlation analysis and found three Magpie descriptors that have a strong correlation with ITC, namely, mean atomic number, mean atomic weight, and mean ground state volume per atom. These descriptors based on the primitive cells of substrates are easy to calculate as soon as the structures are optimized, which provide a new route for quickly screening potential substrates from large-scale material pools for high-performance interfacial thermal management of HEMT devices.

AUTHOR DECLARATIONS

Conflict of Interest

The authors have no conflicts to disclose.

Author Contributions

Mohammed Al-Fahdi: Data curation (lead); Formal analysis (lead); Investigation (lead); Methodology (lead); Validation (lead); Visualization (lead); Writing – original draft (lead); Writing – review & editing (supporting). **Ming Hu:** Conceptualization (lead); Formal analysis (supporting); Funding acquisition (lead); Project administration (lead); Resources (lead); Supervision (lead); Writing – review & editing (lead).

DATA AVAILABILITY

The data that support the findings of this study are available from the corresponding author upon reasonable request. The fused OFM+magpie CNN model code is available free of charge at https://github.com/Mofahdi/OFM-magpie-CNN-Model-for_ITC_prediction. The almaBTE scripts and tutorials are available free of charge at https://github.com/Mofahdi/almaBTE_io.

REFERENCES

[1] J. Zhu, D. Tang, W. Wang, J. Liu, K. W. Holub, and R. Yang, "Ultrafast thermoreflectance techniques for measuring thermal conductivity and interface thermal conductance of thin films," J. Appl. Phys. **108**, 094315 (2010).

[2] X. Wu, Y. Ni, J. Zhu, N. D. Burrows, C. J. Murphy, T. Dumitrica, and X. Wang, "Thermal transport across surfactant layers on gold nanorods in aqueous solution," ACS Appl. Mater. Interfaces **8**(16), 10581–10589 (2016).

[3] Z. Chang, J. Ma, K. Yuan, J. Zheng, B. Wei, M. Al-Fahdi, Y. Gao, X. Zhang, H. Shao, M. Hu, and D. Tang, "Zintl phase compounds Mg3Sb2−xBix (x = 0, 1, and 2) monolayers: Electronic, phonon and thermoelectric properties from *Ab initio* calculations," Front. Mech. Eng. **8**, 876655 (2022).

[4] D. G. Cahill, P. V. Braun, G. Chen, D. R. Clarke, S. Fan, K. E. Goodson, P. Keblinski, W. P. King, G. D. Mahan, A. Majumdar, H. J. Maris, S. R. Phillpot, E. Pop, and L. Shi, "Nanoscale thermal transport. II. 2003–2012," Appl. Phys. Rev. **1**(1), 011305 (2014).

[5] Z. Tian, K. Esfarjani, and G. Chen, "Enhancing phonon transmission across a Si/Ge interface by atomic roughness: First-principles study with the green's function method," Phys. Rev. B **86**(23), 235304 (2012).

[6] N. R. Scott, D. L. Stoddard, M. D. Nelms, Z. Wallace, I. Turner, L. Turner, M. Croom, K. Franklin, S. Sandifer, M. S. Ali Al-fahdi, T. Butler, and A. M. Rajendran, "Experimental and computational characterization of glass microsphere-cementitious composites," Cement Concrete Res. **152**, 106671 (2022).

[7] W. A. Little, "The transport of heat between dissimilar solids at low temperatures," Can. J. Phys. **37**, 334–349 (1959).

[8] E. T. Swartz and R. O. Pohl, "Thermal boundary resistance," Rev. Mod. Phys. **61**, 605–668 (1989).

[9] H. S. Park and J. Punch, "Friction factor and heat transfer in multiple microchannels with uniform flow distribution," Int. J. Heat Mass Transfer **51**, 4535–4543 (2008).

[10] D. B. Tuckerman and R. F. Pease, "Optimized convective cooling using micromachined structures," J. Electrochem. Soc. **129**, C98 (1982).

[11] Y. Zhang, D. Ma, Y. Zang, X. Wang, and N. Yang, "A modified theoretical model to accurately account for interfacial roughness in predicting the interfacial thermal conductance," Front. Energy Res. **6**, 48 (2018).

[12] Y. Zhou, X. Zhang, and M. Hu, "Quantitatively analyzing phonon spectral contribution of thermal conductivity based on nonequilibrium molecular dynamics simulations. I. From space Fourier transform," Phys. Rev. B **92**(19), 195204 (2015).

[13] Y. Zhou and M. Hu, "Quantitatively analyzing phonon spectral contribution of thermal conductivity based on nonequilibrium molecular dynamics simulations. II. From time Fourier transform," Phys. Rev. B **92**(19), 195205 (2015).

[14] J. Dai and Z. Tian, "Rigorous formalism of anharmonic atomistic green's function for three-dimensional interfaces," Phys. Rev. B **101**(4), 041301 (2020).

[15] J.-S. Wang, J. Wang, and N. Zeng, "Nonequilibrium reen's function approach to mesoscopic thermal transport," Phys. Rev. B **74**(3), 033408 (2006).

01. June 2024 08:58:00

[16]P. Reddy, K. Castelino, and A. Majumdar, "Diffuse mismatch model of thermal boundary conductance using exact phonon dispersion," Appl. Phys. Lett. **87**(21), 211908 (2005).

[17]D. B. Brown, T. L. Bougher, X. Zhang, P. M. Ajayan, B. A. Cola, and S. Kumar, "Thermal boundary conductance and phonon transmission in hexagonal boron nitride/graphene heterostructures," Phys. Status Solidi A **216**(23), 1900446 (2019).

[18]M. Al-Fahdi, T. Ouyang, and M. Hu, "High-throughput computation of novel ternary B–C–N structures and carbon allotropes with electronic-level insights into superhard materials from machine learning," J. Mater. Chem. A **9**(48), 27596–27614 (2021).

[19]J. Ojih, M. Al-Fahdi, A. D. Rodriguez, K. Choudhary, and M. Hu, "Efficiently searching extreme mechanical properties via boundless objective-free exploration and minimal first-principles calculations," npj Comput. Mater. **8**(1), 143 (2022).

[20]W. Xia, M. Sakurai, B. Balasubramanian, T. Liao, R. Wang, C. Zhang, H. Sun, K.-M. Ho, J. R. Chelikowsky, D. J. Sellmyer, and C.-Z. Wang, "Accelerating the discovery of novel magnetic materials using machine learning–guided adaptive feedback," Proc. Natl. Acad. Sci. U.S.A. **119**(47), e2204485119 (2022).

[21]A. Rodriguez, C. Lin, H. Yang, M. Al-Fahdi, C. Shen, K. Choudhary, Y. Zhao, J. Hu, B. Cao, H. Zhang, and M. Hu, "Million-scale data integrated deep neural network for phonon properties of heuslers spanning the periodic table," npj Comput. Mater. **9**(1), 20 (2023).

[22]A. Rodriguez, C. Lin, C. Shen, K. Yuan, M. Al-Fahdi, X. Zhang, H. Zhang, and M. Hu, "Unlocking phonon properties of a large and diverse set of cubic crystals by indirect bottom-up machine learning approach," Commun. Mater. **4**(1), 61 (2023).

[23]J. Ojih, M. Al-Fahdi, Y. Yao, J. Hu, and M. Hu, "Graph theory and graph neural network assisted high-throughput crystal structure prediction and screening for energy conversion and storage," J. Mater. Chem. A **12**(14), 8502–8515 (2024).

[24]M. Al-Fahdi, A. Rodriguez, T. Ouyang, and M. Hu, "High-throughput computation of new carbon allotropes with diverse hybridization and ultrahigh hardness," Crystals **11**(7), 783 (2021).

[25]A. Talapatra, B. P. Uberuaga, C. R. Stanek, and G. Pilania, "Band gap predictions of double perovskite oxides using machine learning," Commun. Mater. **4**(1), 46 (2023).

[26]G. Wang and Y. Zhou, "Thermal management modeling for β-Ga2O3-highly thermal conductive substrates heterostructures," IEEE Trans. Compon. Packag. Manuf. Technol. **12**(4), 638–646 (2022).

[27]R. Singh, T. R. Lenka, D. K. Panda, and H. P. Nguyen, "Investigation of β-Ga2O3-based hemts using 2D simulations for low noise amplification and RF applications," ERX **3**(3), 035042 (2021).

[28]Y. Zhao, E. M. Siriwardane, Z. Wu, N. Fu, M. Al-Fahdi, M. Hu, and J. Hu, "Physics guided deep learning for generative design of crystal materials with symmetry constraints," npj Comput. Mater. **9**(1), 38 (2023).

[29]Y. Zhao, M. Al-Fahdi, M. Hu, E. M. D. Siriwardane, Y. Song, A. Nasiri, and J. Hu, "High-throughput discovery of novel cubic crystal materials using deep generative neural networks," Adv. Sci. **8**(20), 2100566 (2021).

[30]G. Qin, Y. Wei, L. Yu, J. Xu, J. Ojih, A. D. Rodriguez, H. Wang, Z. Qin, and M. Hu, "Predicting lattice thermal conductivity from fundamental material properties using machine learning techniques," J. Mater. Chem. A **11**(11), 5801–5810 (2023).

[31]J. Ojih, A. Rodriguez, J. Hu, and M. Hu, "Screening outstanding mechanical properties and low lattice thermal conductivity using global attention graph neural network," Energy AI **14**, 100286 (2023).

[32]J. Ojih, C. Shen, A. Rodriguez, H. Zhang, K. Choudhary, and M. Hu, "High-throughput computational discovery of 3218 ultralow thermal conductivity and dynamically stable materials by dual machine learning models," J. Mater. Chem. A **11**(44), 24169–24183 (2023).

[33]J. E. Saal, S. Kirklin, M. Aykol, B. Meredig, and C. Wolverton, "Materials design and discovery with high-throughput density functional theory: The open quantum materials database (OQMD)," JOM **65**(11), 1501–1509 (2013).

[34]G. Kresse and J. Furthmüller, "Efficiency of AB-initio total energy calculations for metals and semiconductors using a plane-wave basis set," Comput. Mater. Sci. **6**(1), 15–50 (1996).

[35]G. Kresse and J. Furthmüller, "Efficient iterative schemes for *Ab initio* total-energy calculations using a plane-wave basis Set," Phys. Rev. B **54**(16), 11169–11186 (1996).

[36]G. Kresse and D. Joubert, "From ultrasoft pseudopotentials to the projector augmented-wave method," Phys. Rev. B **59**(3), 1758–1775 (1999).

[37]J. P. Perdew, K. Burke, and M. Ernzerhof, "Generalized gradient approximation made simple," Phys. Rev. Lett. **77**(18), 3865–3868 (1996).

[38]P. E. Blöchl, "Projector augmented-wave method," Phys. Rev. B **50**(24), 17953–17979 (1994).

[39]H. J. Monkhorst and J. D. Pack, "Special points for Brillouin-zone integrations," Phys. Rev. B **13**(12), 5188–5192 (1976).

[40]F. Zhou, W. Nielson, Y. Xia, and V. Ozoliņš, "Lattice anharmonicity and thermal conductivity from compressive sensing of first-principles calculations," Phys. Rev. Lett. **113**, 185501 (2014).

[41]F. Zhou, W. Nielson, Y. Xia, and V. Ozoliņš, "Compressive sensing lattice dynamics. I. General formalism," Phys. Rev. B **100**, 184308 (2019).

[42]F. Zhou, B. Sadigh, D. Åberg, Y. Xia, and V. Ozoliņš, "Compressive sensing lattice dynamics. II. Efficient phonon calculations and long-range interactions," Phys. Rev. B **100**, 184309 (2019).

[43]A. Togo and I. Tanaka, "First principles phonon calculations in materials science," Scr. Mater. **108**, 1–5 (2015).

[44]W. Li, J. Carrete, N. A. Katcho, and N. Mingo, "Shengbte: A solver of the Boltzmann transport equation for phonons," Comput. Phys. Commun. **185**(6), 1747–1758 (2014).

[45]Z. Yan and S. Kumar, "Phonon mode contributions to thermal conductivity of pristine and defective β-Ga2O3," Phys. Chem. Chem. Phys. **20**(46), 29236–29242 (2018).

[46]J. Carrete, B. Vermeersch, A. Katre, A. van Roekeghem, T. Wang, G. K. H. Madsen, and N. Mingo, "Almabte : A solver of the space–time dependent Boltzmann transport equation for phonons in structured materials," Comput. Phys. Commun. **220**, 351–362 (2017).

[47]L. Ward, A. Dunn, A. Faghaninia, N. E. R. Zimmermann, S. Bajaj, Q. Wang, J. Montoya, J. Chen, K. Bystrom, M. Dylla *et al.*, "Matminer: An open source toolkit for materials data mining," Comput. Mater. Sci. **152**, 60–69 (2018).

[48]L. Ward, A. Agrawal, A. Choudhary, and C. Wolverton, "A general-purpose machine learning framework for predicting properties of inorganic materials," npj Comput. Mater. **2**, 16028 (2016).

[49]T. Lam Pham, H. Kino, K. Terakura, T. Miyake, K. Tsuda, I. Takigawa, and H. Chi Dam, "Machine learning reveals orbital interaction in materials," Sci. Technol. Adv. Mater. **18**, 756–765 (2017).

[50]M. Al-Fahdi, K. Yuan, Y. Yao, R. Rurali, and M. Hu, "High-throughput thermoelectric materials screening by deep convolutional neural network with fused orbital field matrix and composition descriptors," Appl. Phys. Rev. **11**(2), 021402 (2024).

[51]R. G. Babu, A. Nedumaran, G. Manikandan, and R. Selvameena, "Tensorflow: Machine learning using heterogeneous edge on distributed systems," Deep Learning in Visual Computing and Signal Processing, 71–90 (2022), available at: https://www.taylorfrancis.com/chapters/edit/10.1201/9781003277224-4/tensorflow-machine-learning-using-heterogeneous-edge-distributed-systems-ganesh-babu-nedumaran-manikandan-selvameena

[52]T. K. Ho, "Random decision forests," in *Proceedings of the 3rd International Conference on Document Analysis and Recognition* (IEEE, 1995), Vol. 1, pp. 278–282.

[53]J. H. Friedman, "Greedy function approximation: A gradient boosting machine," Ann. Statist. **29**, 1189–1232 (2001).

[54]F. Pedregosa, G. Varoquaux, A. Gramfort, V. Michel, B. Thirion, O. Grisel, M. Blondel, P. Prettenhofer, R. Weiss, and V. Dubourg, "Scikit-learn: Machine learning in python," J. Mach. Learn. Res. **12**(85), 2825–2830 (2011).

[55]W. Kirch, "Pearson's correlation coefficient," Encyclopedia of Public Health, 1090–1091 (2008), available at: https://link.springer.com/referenceworkentry/10.1007/978-1-4020-5614-7_2569

[56]M. Al-Fahdi, X. Zhang, and M. Hu, "Phonon transport anomaly in metavalent bonded materials: Contradictory to the conventional theory," J. Mater. Sci. **56**(33), 18534–18549 (2021).

[57]Z. Chang, K. Yuan, J. Li, Z. Sun, J. Zheng, M. Al-Fahdi, Y. Gao, B. Wei, X. Zhang, M. Hu, and D. Tang, "Anomalous thermal conductivity induced by high dispersive optical phonons in rubidium and cesium halides," EES **16**, 30–39 (2022).

01. June 2024 08:58:00